Journal of Materials Chemistry B

ROYAL SOCIETY OF CHEMISTRY

PAPER

View Article Online
View Journal | View Issue

Cite this: *J. Mater. Chem. B*, 2020, **8**, 4469

Fluorinated porphyrin-based theranostics for dual imaging and chemo-photodynamic therapy†

Huaibin Zhang,[ab] Shaowei Bo,[a] Kai Zeng,[a] Jie Wang,[a] Yu Li,[b] Zhigang Yang,[a] Xin Zhou,*[b] Shizhen Chen*[b] and Zhong-Xing Jiang*[a]

Received 10th January 2020,
Accepted 14th April 2020

DOI: 10.1039/d0tb00083c

rsc.li/materials-b

Convenient strategies to transform regular liposomes or nano-micelles into multifunctional theranostics would be highly valuable in cancer therapy. Herein, we developed an amphiphilic fluorinated porphyrin dendrimer as a multifunctional "add-on" module which would self-assemble onto liposomal drug delivery systems and conveniently transform the liposomes into novel theranostics. Through cancer cells and murine xenograft tumor model assays, the theranostics showed valuable fluorescence/^{19}F magnetic resonance dual modal imaging and highly efficient chemo-photodynamic therapy. The modular strategy facilitates the convenient and standardized preparation of multifunctional theranostics.

Introduction

The integration of multimodal imaging and multiple therapeutic agents into theranostics is highly attractive in cancer therapy because it may achieve high therapeutic efficacy through comprehensive tumor-drug image guided combination therapy.[1] On the therapy side, combination cancer therapy, treating cancer with multiple therapeutic agents, has been approved in clinics to efficiently eliminate cancer cells through multiple mechanisms and reduce drug resistance.[2] In recent years, photodynamic therapy (PDT) has become a promising complement to chemotherapy because of its non-invasiveness, low toxicity, repeatability and avoidance of multi-drug resistance.[3] On the imaging side, theranostics with multimodal imaging takes advantage of each imaging technology and provides comprehensive multi-dimensional drug-tumor-therapy images for accurate cancer diagnosis and therapy.[1] Among the various imaging modalities, the combination of fluorescence imaging (FL) and ^{19}F magnetic resonance imaging (^{19}F MRI) is highly valuable.[4] FL provides high intensity and real-time images in a convenient and well established way, but it suffers the poor penetration of light in deep tissues, while ^{19}F MRI complements FL by providing "hot spot" images without background signals, ionizing radiations, and tissue depth limits.[5] Therefore, it would be highly beneficial for cancer therapy to incorporate chemotherapy, PDT, FL, and ^{19}F MRI into novel theranostics.

However, it would be very challenging to develop such theranostics. First, the relatively low sensitivity of ^{19}F MRI requires a number of ^{19}F molecules with similar chemical shifts to achieve high local ^{19}F concentration,[4,6] which would lead to difficulties in the synthesis of ^{19}F MRI agents. Second, the low water solubility and strong aggregation of conventional fluorescent agents, PDT photosensitizers and ^{19}F MRI agents would result in signal quenches, low therapeutic efficacy, formulation issues, *etc.*[4a,5,7] Third, it is difficult to synchronize the drug delivery, release and PDT processes with imaging technologies due to the off-target and premature drug/photosensitizer release issues. To address these issues, a fluorinated amphiphilic porphyrin dendrimer F-PP with FL, ^{19}F MRI, and PDT capabilities was herein developed as a multifunctional module for the convenient construction of liposomal theranostics (Fig. 1). Besides its multifunction, F-PP may be a convenient "add-on" module for the existing drug delivery systems (liposomes, micelles, dendrimers, *etc.*)[8] and transform them into theranostics with multimodal imaging and multiple therapeutic agents by self-assembling onto the nanoparticle surface.

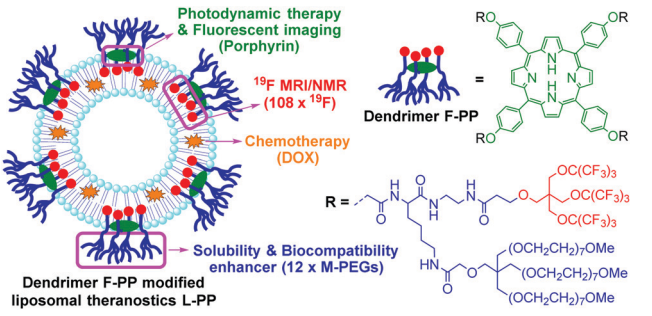

Fig. 1 Dendrimer F-PP as an "add-on" module for theranostic L-PP.

[a] *Hubei Province Engineering and Technology Research Center for Fluorinated Pharmaceuticals and School of Pharmaceutical Sciences, Wuhan University, Wuhan 430071, China. E-mail: zxjiang@whu.edu.cn*

[b] *State Key Laboratory for Magnetic Resonance and Atomic and Molecular Physics, Wuhan Institute of Physics and Mathematics, Chinese Academy of Sciences, Wuhan 430071, China. E-mail: xinzhou@wipm.ac.cn*

† Electronic supplementary information (ESI) available. See DOI: 10.1039/d0tb00083c

F-PP contained 3 structural and functional moieties which were connected through 4 L-lysines: a tetrabenzylporphyrin core as both a fluorescent chromophore and a PDT photosensitizer, 4 highly fluorinated dendrons with 108 symmetrical ^{19}F as strong ^{19}F MRI signal emitters, and 4 highly branched monodisperse polyethylene glycols (M-PEGs) as solubility and biocompatibility enhancers. As a water soluble non-ionic amphiphile, F-PP could on one hand avoid the FL and ^{19}F MRI signal quenches and improve the PDT efficacy by relieving the strong aggregation of porphyrin and fluorocarbons, and on the other hand easily "add-on" to doxorubicin (DOX) loaded liposomes through self-assembly onto the lipid bilayer.[9] In addition, when F-PP was anchored on the nanoparticle surface with its 4 hydrophobic fluorinated dendrons, its 12 M-PEGs would PEGylate the liposomes. In these means, a multifunctional theranostics for imaging-guided cancer therapy would be conveniently prepared.

Experimental

Cellular uptake of F-PP and L-PP

The cellular uptake of F-PP was detected in HepG2 cells using a confocal microscope. Briefly, HepG2 cells were seeded into confocal dishes and incubated at 37 °C for 24 h. Then the medium was removed and replaced with F-PP medium (5 mg mL^{-1}). After 2 h of incubation, the medium was removed and washed with PBS buffer, followed by DAPI staining of the nuclei for 5 min, and then imaged using a confocal microscope. The cellular uptake of DOX and L-PP followed the same procedure.

Detection of singlet oxygen *in vitro*

HepG2 cells were seeded in a 6-well plate at a density of 2×10^5 mL^{-1}, and incubated with L-PP (10 μM F-PP) at 37 °C for 2 h. After washing with PBS, the cells were incubated with carboxy-H_2DCFDA (25 μM) for 30 min, then washed again with PBS and irradiated with a 650 nm laser at a power density of 100 mW cm^{-2} for 5 min per well. The cells were fixed with 4% formaldehyde polymer for 10 min and washed with PBS 3 times. Finally, the cells were imaged under a confocal laser scanning microscope (A1R/A1, Nikon, Japan).

In vitro phototoxicity

HepG2 cells were seeded into 96-well plates and incubated for 12 h. The cells were incubated with DOX and L-PP (0, 0.5, 1, 2, 5 and 10 μg mL^{-1} DOX) for 24 h at 37 °C respectively. After being washed with PBS, the cells were irradiated with a 650 nm laser at a power density of 100 mW cm^{-2} for 5 min. The non-irradiation group was kept under the same conditions except for irradiation. A methylthiazolytetrazolium (MTT) assay kit was employed to evaluate cell toxicity.

For staining of live and dead cells, the cells were seeded in a 6-well plate and incubated with L-PP (10 μM F-PP) at 37 °C for 2 h, washed with PBS and irradiated with a 650 nm laser at a power density of 100 mW cm^{-2} for 10 min. Then the cells were incubated with calcein AM (4 μM) and propidium iodide (4 μM) for 30 min and 5 min, respectively. Cellular fluorescence images were obtained by a Confocal Laser Scanning Microscope (A1R/A1, Nikon, Japan).

In vivo ^{19}F MRI experiments

HepG2 tumor bearing Balb/c nude mice were purchased from Cloud-Clone Corp. (CCC, Wuhan) and used for the *in vivo* evaluation of L-PP. In this study, mice were injected with 250 μL L-PP (42.4 μM kg^{-1} of F-PP) *via* the tail vein and anesthetized using isoflurane. All animal experimental procedures, including *in vivo* ^{19}F MRI experiments, fluorescence imaging, chemotherapy and phototherapy, were performed in accordance with the National Institutes of Health Guide for the Care and Use of Laboratory Animals and were approved by the Institutional Animal Care and Use Committee of Wuhan University. ^1H MRI: method = RARE, matrix size = 256 × 256, FOV = 40 mm × 30 mm, TR = 2500 ms, TE = 33 ms, RARE factor = 8, number of average = 4, scan time = 80 s; ^{19}F MRI: method = RARE, Matrix size = 32 × 32, FOV = 40 mm × 30 mm, TR = 1600 ms, TE = 2.95 ms, RARE factor = 4, number of average = 64, scan time = 13 min.

Fluorescence imaging

For *in vivo* experiments, 250 μL of L-PP (42.4 μM kg^{-1} of F-PP) were intravenously injected into the HepG2 tumor-bearing mice and the fluorescence images were obtained at 4 h, 8 h, 12 h, 24 h, and 48 h, respectively. Fluorescence imaging of organs were obtained from the organs collected from sacrificed mice after the 48 h *in vivo* imaging. The fluorescence scans were recorded on an IVIS spectrum system. Fluorescence imaging was performed using a 640 nm excitation filter and a 720 nm emission filter.

In vivo chemotherapy and phototherapy

HepG2 tumor bearing Balb/c nude mice were divided into 4 treatment groups: (1) saline, (2) DOX, (3) L-PP, and (4) L-PP + laser. The 4 groups of mice were injected through the tail vein on day 0, 3, 6, respectively. The DOX doses for the DOX group, the L-PP group and the L-PP + laser group were 5 mg kg^{-1} and the F-PP doses for the L-PP group and the L-PP + laser group were 3 μM kg^{-1}, respectively. Twelve hours post L-PP injection, the mice in group 4 was irradiated with a 650 nm laser at a power density of 100 W cm^{-2} for 10 min. The body weight and tumor volume of mice were measured every 2 days for a period of 21 days. The tumour volume was calculated according to the formula, volume = (width^2 × length)/2.

Results and discussion

Synthesis and physicochemical properties of F-PP

Dendrimer F-PP was synthesized in a convergent way on a gram scale and fully characterized using HPLC, $^{19}F/^1H/^{13}C$ NMR, and MS (ESI†). F-PP gave a singlet ^{19}F NMR peak at −72.34 ppm from its 108 symmetrical ^{19}F (Fig. 2a), distinctive concentration-dependent UV absorption at 420 nm, 517 nm, 554 nm, 595 nm,

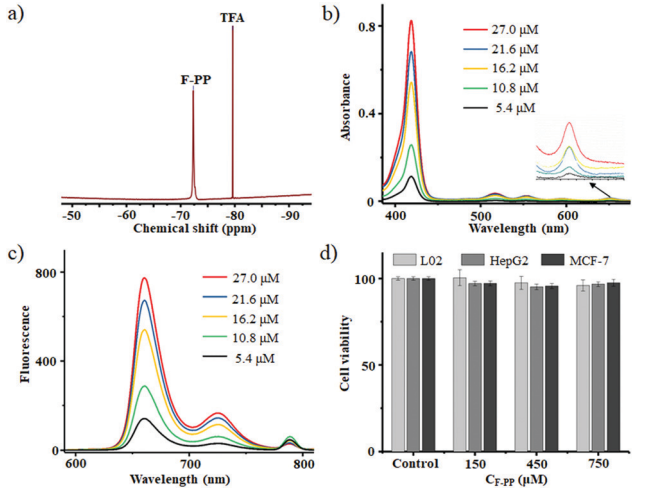

Fig. 2 ^{19}F NMR (a, 376 MHz, in water, TFA as an internal standard), concentration-dependent UV absorption (b, in water) and fluorescence emission (c, in water), and biocompatibility assay (d) of F-PP.

and 651 nm (Fig. 2b), and fluorescence emission at 660 nm, 725 nm, and 788 nm (Fig. 2c). Although it contained highly hydrophobic fluorinated dendrons and tetrabenzylporphyrin, F-PP is freely soluble in water because of its 12 hydrophilic M-PEGs. Notably, F-PP had a low self-aggregation tendency in water because no detectable nanoparticle was found using dynamic light scattering (DLS), which was further confirmed by the solvent-dependent UV absorption, fluorescence emission and ^{19}F NMR of F-PP (ESI†). Such non-aggregative behaviour of the fluorinated dendrimer was also reported by Yu *et al.*[9] Because of its excellent solubility and low aggregation tendency in water, aggregation-induced self-quenching, which is a major issue in porphyrins-based FL and PDT agents, was not observed in F-PP. Importantly, even at high concentrations, F-PP exhibited high biocompatibility toward a series of cell lines, including L02 cells, HepG2 cells and MCF-7 cells (Fig. 2d). Here, the M-PEGs in F-PP played a crucial role in its high biocompatibility.

In vitro imaging and cell uptake

The designed liposomal theranostic L-PP was formulated through a film dispersion method with both hydrogenated soybean phosphatidylcholine (HSPC) and F-PP as the surfactants, cholesterol as an additive, and DOX as the chemotherapy drug. A DOX encapsulation efficiency of 86% and a DOX loading content of 6% were obtained for L-PP (ESI†). DLS of L-PP showed a particle size of 121 nm and a polydispersity index of 0.146 (Fig. 3a). L-PP exhibited good stability over 15 days and a pH sensitive drug release profile (ESI†). As expected, all the ^{19}F molecules in L-PP accumulatively gave a strong singlet ^{19}F NMR peak at −72.61 ppm (Fig. 3b) with pretty short ^{19}F relaxation times (ESI,† F-PP: T_1 = 375 ms, T_2 = 10 ms; L-PP: T_1 = 439 ms, T_2 = 9 ms, at 376 MHz), which facilitated 100% ^{19}F utilization and rapid data collection time for highly sensitive ^{19}F MRI. A detectable concentration of 99 μM F-PP (or 10.7 mM ^{19}F) with a scan time of 160 seconds was achieved for L-PP in ^{19}F MRI phantom experiments (Fig. 3c). It is noteworthy that ^{19}F MRI signal intensities (SI) of F-PP and L-PP

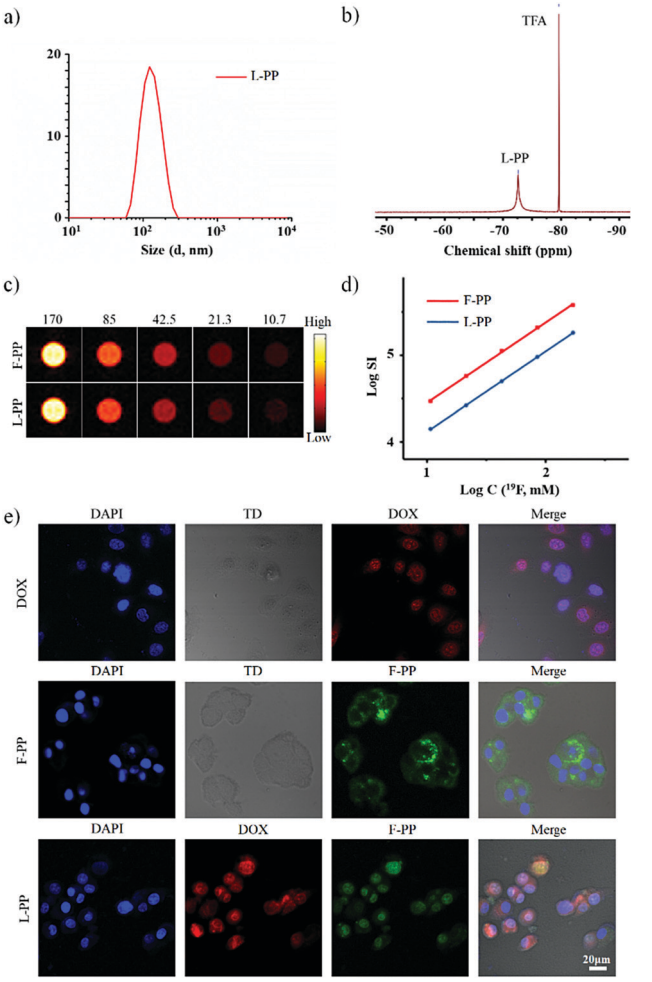

Fig. 3 DLS (a) and ^{19}F NMR (b, 376 MHz, in water, TFA as an internal standard) of L-PP, ^{19}F MRI (c, in water) and SI *versus* C(^{19}F) plot (d) of L-PP and F-PP, and confocal images of HepG2 cells after 2 h of treatment with DOX, F-PP or L-PP (e).

are proportional to their ^{19}F concentrations, respectively (Fig. 3d), which would be valuable for quantifying F-PP and L-PP with the ^{19}F MRI signal intensity. Confocal microscopy images of L-PP treated HepG2 cells indicated that both F-PP and DOX were efficiently delivered into the cells, especially in the nucleus (Fig. 3e). In contrast, F-PP was mainly distributed in the cytoplasm of F-PP treated HepG2 cells (ESI†). Notably, the "add-on" of F-PP in L-PP was confirmed by both the ^{19}F NMR chemical shift change from −72.34 ppm in F-PP to −72.61 ppm in L-PP and no detection of unencapsulated F-PP from Micro-spin G-50 column treated L-PP.

The photodynamic properties of theranostic L-PP

The PDT effect and cytotoxicity of L-PP were investigated in HepG2 cells. First, using a commercial probe 6-carboxy-2′,7′-dichlorodihydrofluorescein diacetate (H_2DCFDA), the reactive oxygen species (ROS) generating ability of L-PP in HepG2 cells was evaluated (Fig. 4a). Without L-PP treatment or 650 nm laser irradiation, negligible ROS in HepG2 cells were detected by the

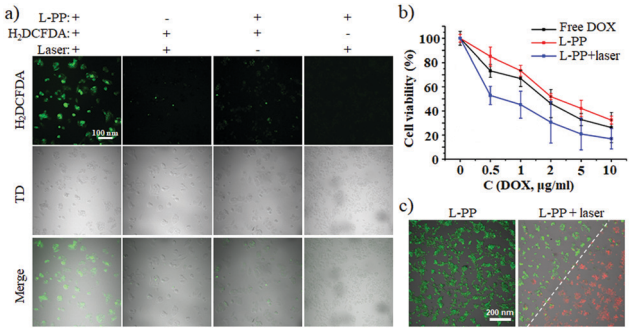

Fig. 4 Confocal images (a), relative viability (b), and fluorescence images of live/dead cell staining (c) of HepG2 cells after 2 h of treatment with the indicated materials. L-PP in (a) and (c) contained 10 μM F-PP. 5 min (a and b) and 10 min (c) of 650 nm laser irradiation at 100 mW cm^{-2} were applied.

green fluorescence of H_2DCFDA, while most HepG2 cells with the treatment of L-PP and 650 nm laser irradiation at 100 mW cm^{-2} for 5 min emitted green fluorescence of H_2DCFDA. So, L-PP can significantly improve the oxidative stress of HepG2 cells with low power density laser irradiation. Second, the cytotoxicity assay showed the high combination therapy efficiency of chemotherapy and PDT (Fig. 4b). Compared to DOX, L-PP showed slightly lower cytotoxicity towards HepG2 cells. The cytotoxicity was dramatically improved by the PDT effect when HepG2 cells were treated with both L-PP and low power density laser irradiation. Third, calcein-AM/PI double staining, in which green fluorescence from calcein-AM represented live cells and red fluorescence from PI represented dead or later apoptosis cells, was employed to assess the PDT enhancement efficacy (Fig. 4c). After 10 min of laser irradiation, most L-PP treated HepG2 cells were killed, which emitted red fluorescence and resulted in a clear border between the live and dead cells around the light spot. Therefore, L-PP successfully integrated the chemotherapy of DOX and the PDT of F-PP for enhanced therapeutic efficacy in cancer cells.

In vivo fluorescence imaging and ^{19}F MRI of HepG2 tumor

The *in vivo* FL and ^{19}F MRI dual imaging of theranostic L-PP was carried out in a xenograft HepG2 liver tumor nude mouse model. First, the biodistribution of L-PP in shallow organs was investigated using FL, which showed the gradual accumulation of L-PP in the tumor region after the tail vein injection of L-PP (Fig. 5a, a dose of 42 μM kg^{-1} F-PP). Second, the accumulation of L-PP in tumor was also investigated with ^{19}F MRI. With an F-PP dose as low as 42 μM kg^{-1}, ^{19}F MRI gave clear "hot spot" images of L-PP in the tumor region (Fig. 5b, tumor containing cross-sections). Compared to FL, ^{19}F MRI provided more detailed and accurate images of L-PP in tumor. The accumulation of L-PP in tumor, especially inside of tumor, was clearly showed by ^{19}F MRI, while FL could hardly show the vivid distribution of L-PP in tumor. Third, the accumulation of L-PP in tumor was quantitatively analysed with the SI of *in vivo* FL and ^{19}F MRI. A peak intensity of L-PP in the tumor at 24 h post-injection was found by both imaging technologies,

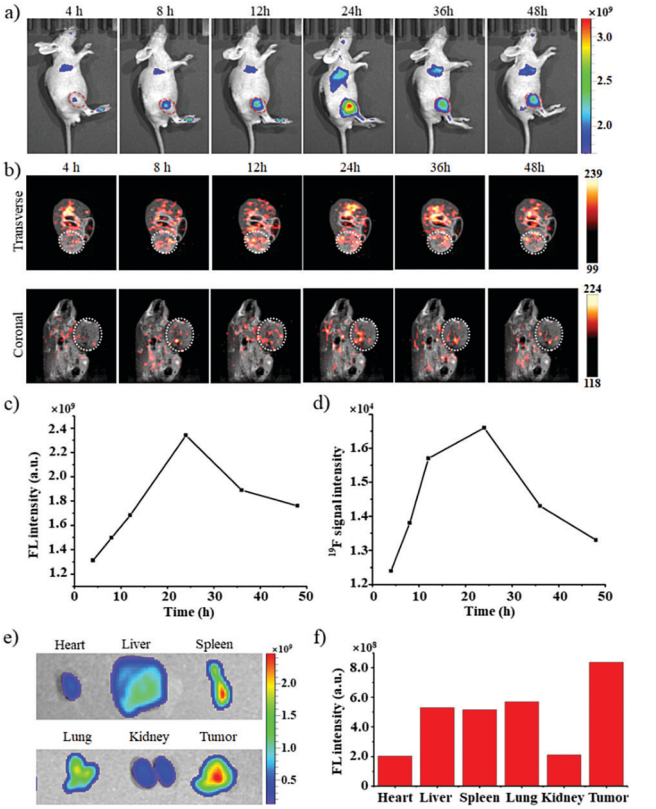

Fig. 5 *In vivo* FL (a), ^{19}F MRI (b, upper: transverse section, lower: coronal section, the tumor was marked with a white dotted circle), tumor region SI curves of FL (c) and ^{19}F MRI (d, transverse section) of mice after intravenous injection of L-PP, *ex vivo* FL (e) and quantitative SI analysis (f) of major organs and tumor collected from mice sacrificed 48 h post-injection.

in which different anesthetics used in the imaging process led to slightly different accumulation profiles (Fig. 5c and 6d). Fourth, the biodistribution of L-PP in tumor and internal organs was further studied with *ex vivo* FL of tumor and organs, which also indicated high tumor accumulation of L-PP (Fig. 5e and f). Thus, the two complementary imaging technologies: FL with high sensitivity and ^{19}F MRI without the tissue depth limit, together provided sensitive, accurate, and quantitative *in vivo formation of L-PP.*

Therapy of HepG2 tumor

With the high tumor accumulation of L-PP, the *in vivo* combination cancer therapy with the DOX-based chemotherapy and F-PP-based PDT of L-PP was investigated in 4 groups of xenograft HepG2 liver tumor mice (n = 5). On day 0, 3 and 6, the mice were treated with saline (negative control), DOX (positive control), L-PP, L-PP plus 650 nm laser irradiation at 100 mW cm^{-2} for 5 min, respectively. First, compared to chemotherapy with DOX or L-PP, the combination therapy with L-PP plus laser irradiation showed significantly enhanced tumor growth inhibition, in which almost no tumor growth was observed during the study (Fig. 6a). Second, due to the toxicity of DOX, the mice in the DOX treatment group showed dramatical body weight loss and all died between day 10 and

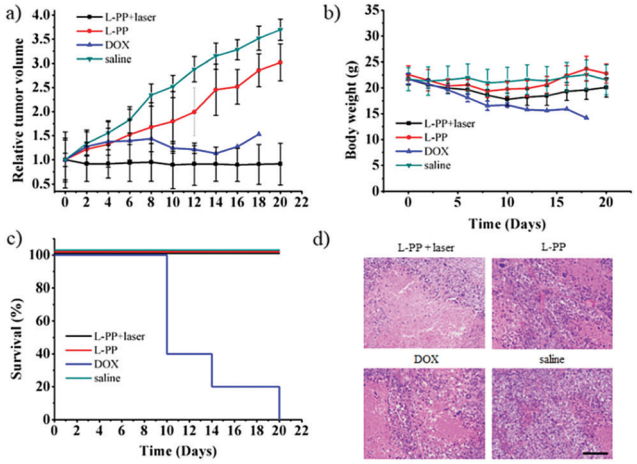

Fig. 6 Tumor growth curves (a), body weight curves (b), and mice survival curves (c) of HepG2 tumor-bearing nude mice after the indicated group treatments, representative H&E staining of tumor after group treatments (d). (Data in (a) and (b) were expressed as mean ± SD, n = 5. Scale bar, 100 μm.)

day 20 (Fig. 6b and c). Although L-PP showed less tumor growth inhibition capability than DOX, the L-PP treatment groups showed dramatically less body weight loss and full survival rate (Fig. 6a–c). Finally, high therapeutic efficacy and lower systematic toxicity were identified for the combination therapy group because much less toxicity to heart, liver, spleen, lungs and kidneys and much higher therapeutic effects on tumor were found by H&E staining of the tissues collected from the mice (Fig. 6d and ESI†).

Conclusions

In summary, we have developed a fluorinated porphyrin dendrimer as an "add-on" module for the convenient construction of multifunctional liposomal theranostics for cancer therapy. The "add-on" module showed valuable fluorescence properties, such as high solubility, high fluorescence intensity, no self-aggregation and aggregation-induced signal quenching, and preferred ^{19}F MRI properties, such as a single ^{19}F NMR peak, short relaxation times, and high ^{19}F MRI sensitivity. The dual imaging modalities complement each other by providing not only highly sensitive and convenient FL of cells and shallow organs, but also the sensitive and quantitative ^{19}F MRI of deep organs without tissue depth limits. It was found that ^{19}F MRI provided much more accurate and vivid *in vivo* images of the drug delivery system in murine. The FL and ^{19}F MRI dual image-guided combination cancer chemotherapy and PDT have been demonstrated in both cancer cells and the murine xenograft tumor model with significantly higher therapeutic efficacy and the overall survival of animals. As it would self-assemble onto liposomal drug delivery systems, the fluorinated porphyrin dendrimer may be employed as a general "add-on" module for various liposomal theranostics, not limited to DOX-loaded liposomes in this case, and provided them with nanoparticle PEGylation, FL, ^{19}F MRI, and PDT for image-guided combination therapy. With this modular strategy, many versatile theranostics may be developed in a simplified, standardized, controllable and precise manner for challenging disease therapy.

Conflicts of interest

The authors have declared that no competing interest exists.

Acknowledgements

We are thankful for financial support from the National Key R&D Program of China (2016YFC1304704, 2018YFA0704000), the National Natural Science Foundation of China (21572168, 91859206, and 81625011), and the Key Research Program of Frontier Sciences, CAS (QYZDY-SSW-SLH018).

Notes and references

1 (*a*) X.-R. Song, S.-X. Yu, S.-H. Li, J. Li, H.-H. Yang, X. Wang, J. Cao, G. Liu and X. Chen, *Adv. Mater.*, 2015, **27**, 3285; (*b*) Q. Chen, X. Wang, C. Wang, L. Feng, Y. Li and Z. Liu, *ACS Nano*, 2015, **9**, 5223; (*c*) J. Mou, T. Lin, F. Huang, H. Chen and J. Shi, *Biomaterials*, 2016, **84**, 13; (*d*) S. Lu, X. Li, M. Shen, X. Shi, J. Zhang and C. Peng, *Adv. Sci.*, 2018, **5**, 1801612; (*e*) B. Yu, H. Wei, Q. He, F. A. Ferreira, C. J. Kutyreff, D. Ni, Z. T. Rosenkrans, L. Cheng, F. Yu, J. Engle, X. Lan and W. Cai, *Angew. Chem., Int. Ed.*, 2018, **57**, 218; (*f*) Y. Li, Y. Wu, J. Chen, J. Wan, C. Xiao, J. Guan, X. Song, S. Li, M. Zhang, H. Cui, T. Li, X. Yang, Z. Li and X. Yang, *Nano Lett.*, 2019, **19**, 5806.

2 (*a*) M. Saad, O. B. Garbuzenko and T. Minko, *Nanomedicine*, 2008, **3**, 761; (*b*) A. Jhaveri, P. Deshpande and V. Torchilin, *J. Controlled Release*, 2014, **190**, 352; (*c*) G. Shim, M.-G. Kim, D. Kim, J. Y. Park and Y.-K. Oh, *Adv. Drug Delivery Rev.*, 2017, **115**, 57; (*d*) S. Shen, M. Liu, T. Li, S. Lin and R. Mo, *Biomater. Sci.*, 2017, **5**, 1367; (*e*) S. Gao, G. Tang, D. Hua, R. Xiong, J. Han, S. Jiang, Q. Zhang and C. Huang, *J. Mater. Chem. B*, 2019, **7**, 709.

3 (*a*) B. M. Luby, C. D. Walsh and G. Zheng, *Angew. Chem., Int. Ed.*, 2019, **58**, 2558 (*Angew. Chem.*, 2019, **131**, 2580); (*b*) S. Mallidi, S. Anbil, A.-L. Bulin, G. Obaid, M. Ichikawa and T. Hasan, *Theranostics*, 2016, **6**, 2458; (*c*) X. Li, S. Lee and J. Yoon, *Chem. Soc. Rev.*, 2018, **47**, 1174; (*d*) X. Li, N. Kwon, T. Guo, Z. Liu and J. Yoon, *Angew. Chem., Int. Ed.*, 2018, **57**, 11522; (*e*) S. Monro, K. L. Colon, H. Yin, J. Roque, P. Konda, S. Gujar, R. P. Thummel, L. Lilge, C. C. Cameron and S. A. McFarland, *Chem. Rev.*, 2019, **119**, 797; (*f*) W. Ma, S. Sha, P. Chen, M. Yu, J. Chen, C. Huang, B. Yu, Y. Liu, L. Liu and Z. Yu, *Adv. Healthcare Mater.*, 2020, **9**, 1901100; (*g*) Y. Xiao, F.-F. An, J. Chen, S. Xiong and X.-H. Zhang, *J. Mater. Chem. B*, 2018, **6**, 3692.

4 (*a*) J. M. Janjic, M. Srinivas, D. K. K. Kadayakkara and E. T. Ahrens, *J. Am. Chem. Soc.*, 2008, **130**, 2832; (*b*) S. Mizukami, R. Takikawa, F. Sugihara, M. Shirakawa and K. Kikuchi, *Angew. Chem., Int. Ed.*, 2009, **48**, 3641; (*c*) B. E. Rolfe, I. Blakey, O. Squires, H. Peng, N. R. B. Boase, C. Alexander,

P. G. Parsons, G. M. Boyle, A. K. Whittaker and K. J. Thurecht, *J. Am. Chem. Soc.*, 2014, **136**, 2413; (*d*) S. Bo, C. Song, Y. Li, W. Yu, S. Chen, X. Zhou, Z. Yang, X. Zheng and Z.-X. Jiang, *J. Org. Chem.*, 2015, **80**, 6360; (*e*) Y. Zhang, S. Bo, T. Feng, X. Qin, Y. Wan, S. Jiang, C. Li, J. Lin, T. Wang, X. Zhou, Z.-X. Jiang and P. Huang, *Adv. Mater.*, 2019, **31**, 1806444; (*f*) J. Zhu, Y. Xiao, H. Zhang, Y. Li, Y. Yuan, Z. Yang, S. Chen, X. Zheng, X. Zhou and Z.-X. Jiang, *Biomacromolecules*, 2019, **20**, 1281.

5 (*a*) J. Ruiz-Cabello, B. P. Barnett, P. A. Bottomley and J. W. Bulte, *NMR Biomed.*, 2011, **24**, 114; (*b*) J. C. Knight, P. G. Edwards and S. J. Paisey, *RSC Adv.*, 2011, **1**, 1415; (*c*) I. Tirotta, V. Dichiarante, C. Pigliacelli, G. Cavallo, G. Terraneo, F. B. Bombelli, P. Metrangolo and G. Resnati, *Chem. Rev.*, 2015, **115**, 1106.

6 (*a*) Z.-X. Jiang, X. Liu, E.-K. Jeong and Y. B. Yu, *Angew. Chem., Int. Ed.*, 2009, **48**, 4755; (*b*) S. Temme, C. Grapentin, C. Quast, C. Jacoby, M. Grandoch, Z. Ding, C. Owenier, F. Mayenfels, J. W. Fischer and R. Schubert, *Circulation*, 2015, **131**, 1405; (*c*) W. Yu, Y. Yang, S. Bo, Y. Li, S. Chen, Z. Yang, X. Zheng, Z.-X. Jiang and X. Zhou, *J. Org. Chem.*, 2015, **80**, 4443; (*d*) Q. Peng, Y. Li, S. Bo, Y. Yuan, Z. Yang, S. Chen, X. Zhou and Z.-X. Jiang, *Chem. Commun.*, 2018, **54**, 6000; (*e*) C. Zhang, S. S. Moonshi, W. Wang, H. T. Ta, Y. Han, F. Y. Han, H. Peng, P. KráL, B. E. Rolfe and J. J. Gooding, *ACS Nano*, 2018, **12**, 9162; (*f*) H. Zhang, Y. Li, S. Chen, Y. Yuan, Z.-X. Jiang and X. Zhou, *ACS Appl. Bio. Mater.*, 2019, **2**, 27.

7 (*a*) M. Ethirajan, Y. Chen, P. Joshi and R. K. Pandey, *Chem. Soc. Rev.*, 2011, **40**, 340; (*b*) X. Xue, A. Lindstrom and Y. Li, *Bioconjugate Chem.*, 2019, **30**, 1585.

8 (*a*) S. Svenson and D. A. Tomalia, *Adv. Drug Delivery Rev.*, 2005, **57**, 2106; (*b*) E. R. Gillies and J. M. J. Fréchet, *Drug Discovery Today*, 2005, **10**, 35; (*c*) R. Duncan, *Nat. Rev. Cancer*, 2006, **6**, 688; (*d*) Y. Geng, P. Dalhaimer, S. Cai, R. Tsai, M. Tewari, T. Minko and D. E. Discher, *Nat. Nanotechnol.*, 2007, **2**, 249; (*e*) A. R. Menjoge, R. M. Kannan and D. A. Tomalia, *Drug Discovery Today*, 2010, **15**, 171.

9 (*a*) M. B. Taraban, Y. Li, F. Yue, E. V. Jouravleva, M. A. Anisimov, Z.-X. Jiang and Y. B. Yu, *RSC Adv.*, 2014, **4**, 54565; (*b*) M. B. Taraban, D. J. Deredge, M. E. Smith, K. T. Briggs, Y. Feng, Y. Li, Z.-X. Jiang, P. L. Wintrode and Y. B. Yu, *RSC Adv.*, 2019, **9**, 1956.

